Journal of Alloys and Compounds 1046 (2025) 184863

Contents lists available at ScienceDirect

Journal of Alloys and Compounds

journal homepage: www.elsevier.com/locate/jalcom

Smart design of porous Ni and Ni–W films with tunable mechanical and magnetic performance

Roger de Paz-Castany [a,1], Nicolau López-Pintó [a,1], Konrad Eiler [a], Gavin B.G. Stenning [b], Annick Hubin [c], Eva Pellicer [a,*], Jordi Sort [a,d]

[a] Physics Department, Universitat Autònoma de Barcelona, Cerdanyola del Vallès, Bellaterra 08193, Spain
[b] ISIS Neutron and Muon Source, Rutherford Appleton Laboratory, Chilton, Oxon OX11 0QX, United Kingdom
[c] SUME Department, Vrije Universiteit Brussel, Brussels, Belgium
[d] Institució Catalana de Recerca i Estudis Avançats (ICREA), Pg. Lluís Companys 23, Barcelona 08010, Spain

ARTICLE INFO

Keywords:
Nickel-tungsten films
Electrodeposition
Colloidal crystal templating
Nanoindentation
Curie temperature
Thermal stability

ABSTRACT

Dense and porous Ni and Ni–W alloy films were fabricated via electrodeposition, with the porous structures produced using colloidal crystal templates composed of 20 and 200 nm polystyrene spheres. The study investigates the effects of tungsten content (6–9 wt%) and porosity on the films' mechanical and magnetic properties, as well as their structural stability at elevated temperatures. From a crystallographic viewpoint, both Ni and Ni–W films exhibited a face-centered cubic (fcc) structure, with the diffraction peaks of the Ni–W films shifted toward lower angles due to the alloying of W with Ni. Interestingly, peak splitting was observed in the porous films, which originated from the confined metal growth between the polystyrene spheres. All films were nanocrystalline, with crystallite sizes in the range of 17 – 46 nm. Tungsten addition to nickel enhanced mechanical hardness but decreased magnetic moment and Curie temperature. Porosity, on the other hand, introduced new magnetic contributions not observed in dense films, including superparamagnetic behavior in the Ni–W films with 200 nm-size porosity. Thermal analysis revealed that the porous Ni–W films were morphologically stable up to 800 K, whereas porosity in pure Ni films degraded at 600 K. These findings highlight the potential of Ni–W coatings with tailored porosity for magnetic microelectromechanical systems and sustainable multi-functional coatings.

1. Introduction

Nanostructured ferromagnetic films are widely studied due to their excellent magnetic and mechanical properties, which make them ideal for a wide range of technological applications, including magnetic data storage, spintronic devices and microelectromechanical systems (MEMS) [1–3]. In recent decades, significant progress has been made in developing various fabrication methods to prepare these materials in thin-film form, including physical vapor deposition, chemical vapor deposition and electrochemical deposition. Among these techniques, electrochemical deposition stands out for its simplicity, cost-effectiveness, scalability, and the precise control it offers over film composition and microstructure [4,5].

Electrodeposition has been successfully employed for the fabrication of a wide range of binary and ternary metallic films, such as Cu–Ni, Fe–Ni, Co–Fe, Ni–Pt, Co–Fe–Ni, and Zn–Ni–Co systems, to name a few [6–8]. These alloy films often exhibit improved mechanical strength and tailored magnetic properties compared to their monometallic counterparts. It is well established that the co-deposition of transition metals allows tuning of critical properties such as hardness, wear resistance, saturation magnetization (M_S), and coercivity (H_C) through careful control of the plating solution composition and electroplating parameters [5,7,9].

Among the various electrodeposited metals, nickel (Ni) films attract considerable attention due to their reasonably good mechanical properties and ferromagnetic behavior. Nevertheless, pure Ni coatings may not always provide sufficient hardness and wear resistance for demanding applications. To overcome these limitations, alloying Ni with other transition metals has been extensively explored to tailor both magnetic and mechanical performance. For example, Ni–Fe and Ni–Co

* Corresponding author.
E-mail address: eva.pellicer@uab.cat (E. Pellicer).
[1] Equally contributed

https://doi.org/10.1016/j.jallcom.2025.184863
Received 31 July 2025; Received in revised form 17 October 2025; Accepted 3 November 2025
Available online 4 November 2025

alloys exhibit enhanced magnetic permeability and tunable anisotropy, strongly influenced by deposition potential, pH, and current waveform [10–13]. The addition of Co typically increases coercivity and modifies texture orientation, while Fe co-deposition can yield soft magnetic films with controlled anisotropy. While these transition-metal additions mainly affect the magnetic response of Ni, alloying with refractory elements such as tungsten (W) or molybdenum (Mo) has emerged as an effective strategy to improve its mechanical performance [14,15]. Specifically, the addition of W to the Ni matrix increases hardness, reduces internal stress, and improves the thermal and corrosion resistance of the films [16]. These features make Ni–W coatings attractive candidates as environmentally friendly alternatives to conventional chromium-based coatings, which are being progressively phased out due to increasing regulations and concerns regarding their toxicity and environmental impact [17,18]. However, the influence of refractory elements on the magnetic behavior of Ni-based systems has been comparatively less explored. The mechanical improvement brought by W, however, comes at the cost of reduced magnetic performance. Since W is a paramagnetic element, increasing its content in Ni films leads to a dilution of the magnetic moment and a reduction in properties such as M_S and Curie temperature (T_C) [19,20]. Balancing mechanical and magnetic properties through precise alloying thus remains a challenge in the design of these multifunctional films.

In parallel, the introduction of macro- and mesoscale porosity is a compelling strategy to further tailor the physical properties of metallic films [21,22]. Porous structures can influence surface area, mechanical strength, and magnetic anisotropy, offering additional versatility for applications such as sensors, actuators, and microelectromechanical systems (MEMS). Although porous Ni films have been previously explored for electrochemical applications [23,24], their detailed mechanical and magnetic characterization, particularly when combined with alloying elements such as W, has received limited attention. While several studies have focused separately on either porous Ni films or dense Ni-W alloys, the combined effect of alloying and controlled porosity on the mechanical and magnetic behavior of electrodeposited Ni-W films has not yet been systematically explored.

Furthermore, systematic studies that compare different porosity scales (e.g., 20 nm vs. 200 nm pores) and directly evaluate their effects on mechanical hardness, elastic modulus, and magnetic behavior are still lacking [25]. For this reason, this work presents a systematic study of electrodeposited Ni and Ni–W films with three distinct structural architectures: dense coatings, mesoporous coatings with 20 nm pores, and macroporous coatings with 200 nm pores. The films were electrodeposited potentiostatically from an aqueous electrolyte, with porous variants fabricated by colloidal templating using polystyrene (PS) spheres [25], in order to maintain comparable chemical composition across the Ni–W series (6–9 wt% W). This approach enables a focused assessment of the individual and combined effects of porosity and W incorporation on mechanical and magnetic performance of the resulting films. The thermal stability of the porous samples was also evaluated, showing that the addition of W aids to retain the porous hierarchy after annealing at 800 K.

The findings of this study not only provide new insights into the structure–property relationships of Ni and Ni–W films but also highlight the potential of these materials as durable and mechanically hard coatings for environmentally friendly alternatives to chromium plating, and as candidates for magnetic MEMS applications where combined large surface area, mechanical strength, thermal stability, and magnetic functionalities are required.

2. Experimental section

2.1. Synthesis

Ni and Ni–W films were electrochemically synthesized in a double-jacketed three-electrode cell connected to a Metrohm Autolab PGSTAT302N potentiostat / galvanostat. A platinum wire was used as the counter electrode (CE), while a double-junction Ag|AgCl reference electrode (Metrohm AG) with 3 M KCl inner and 1 M Na_2SO_4 outer solution served as the reference electrode (RE).

For the deposition of dense films, a constant potential of −1.2 V vs. Ag|AgCl (3 M KCl) was applied for 30 min in a gluconate-based electrolyte containing 0.11 M $NiSO_4{\cdot}7H_2O$, 0.5 M sodium gluconate ($NaC_6H_{11}O_7$), and 0.65 M H_3BO_3, adjusted to pH 5.0. For the synthesis of the Ni-W samples, 0.05 M $Na_2WO_4{\cdot}2H_2O$ was also added to the electrolyte. Ti/Au-sputtered silicon chips, with an exposed area of 1 cm^2, acted as the working electrode (WE). Ti (10 nm) served as adhesion layers, while Au (90 nm) ensured the electrical conductivity of the substrate.

Porous Ni and Ni–W films were obtained by means of the colloidal crystal templating method from the same electrolyte. One droplet of a commercial aqueous suspension of PS spheres (either 20 nm diameter beads in a 1 wt% suspension from Thermo Scientific, or 200 nm diameter beads in a 2.5 wt% suspension from Polysciences) was deposited on the Si/Ti/Au substrate, followed by the addition of two drops of Milli-Q water to ensure homogeneous spreading. The substrates were then placed on a hot plate at 40 °C to facilitate solvent evaporation and promote PS self-assembly. Electrodeposition was conducted on the PS-patterned Si/Ti/Au substrates at 25 °C under an applied potential of −1.2 V for 10 min. The deposition templating sequence was repeated three times up to a total deposition time of 30 min to ensure uniform porosity and aiming to obtain ~1.5 μm thick layer, comparable to that of the dense counterparts. PS spheres were subsequently removed by immersion in tetrahydrofuran (THF) for one week. The final thickness of the metallic films was later corroborated by mechanical profilometry (KLA Tencor P-15).

2.2. Compositional, morphological, and structural characterization

Elemental composition of the samples was determined by inductively coupled plasma optical emission spectroscopy (ICP-OES) (Agilent 5900) performed on the same specimens used for magnetic characterization. The samples were digested in a solution of concentrated HF, HCl and HNO_3. Field-emission scanning electron microscopy (FESEM) was performed using a Zeiss Merlin microscope to examine the grain morphology and pore topology. All samples were observed without an additional conductive coating. Atomic force microscopy (AFM) was performed by means of an Atomic Force Microscope from Oxford Instruments to image and determine the mean roughness of the films in taping mode, by scanning areas of 5 μm × 5 μm.

The crystalline structure of the samples was characterized using grazing incidence X-ray diffraction (GIXRD). GIXRD patterns were recorded with a Cu K_α radiation source ($\lambda = 1.541862$ Å), operating at 45 kV and 200 mA. The grazing incidence angle (ω) was fixed at 0.75°, and the 2θ range was measured between 30° and 100°, with a step size of 0.01°. Rietveld refinement was performed using the '*Materials Analysis Using Diffraction*' (MAUD) software to analyze the diffraction patterns and determine the lattice parameters, average crystallite size, microstrains, and phase percentages [26,27]

Morphological changes induced by thermal treatments were assessed by FESEM using a FEI Magellan microscope. An inert Ar atmosphere was used to prevent spontaneous oxidation during the annealing. Samples were heated from 298 K to target temperatures of 400, 500, 600, 700, and 800 K at a constant rate of 5 K/min, subsequently taking FESEM images after each annealing step. At each temperature, the sample was held isothermally for 1 min before being cooled down to room temperature.

2.3. Nanomechanical measurements

Mechanical properties of dense and porous Ni and Ni–W films were evaluated by instrumented nanoindentation using an Anton Paar NHT^2 nanoindenter equipped with a Berkovich pyramidal-shaped diamond

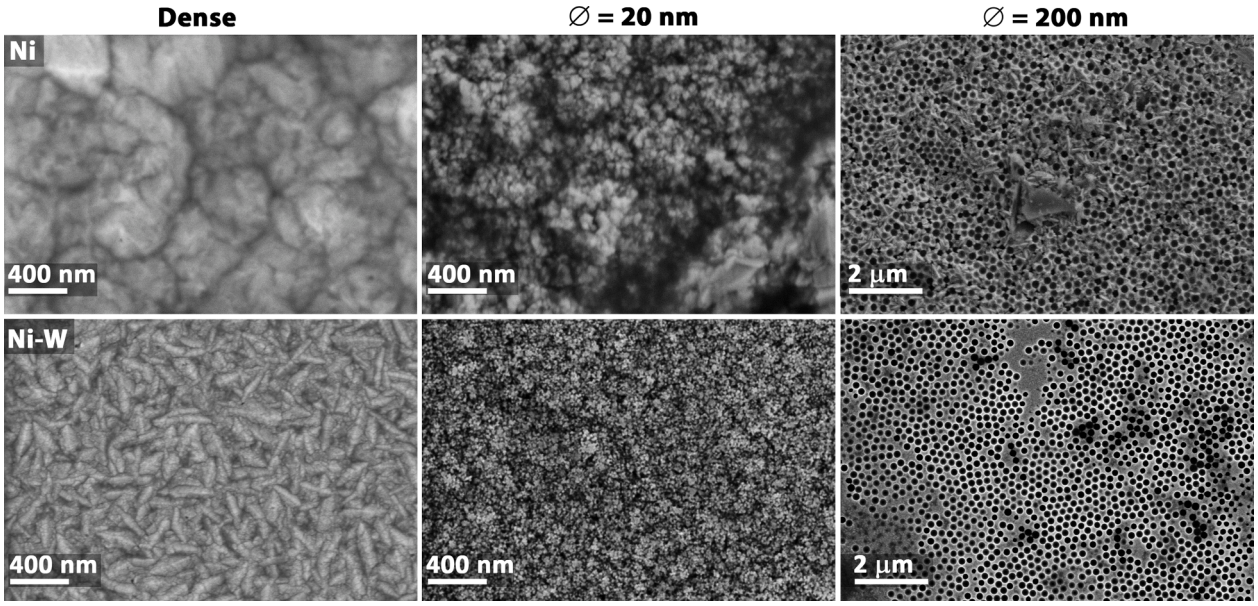

Fig. 1. FESEM images of Ni films with dense, 20 nm pore size and 200 nm pore size morphologies (first row) and the same for the Ni–W counterparts (second row), after electrodeposition and PS spheres removal for the porous cases.

tip. A maximum load of 1.5 mN was applied. Indentation depths ranged from 60 to 180 nm, well within the 10 % film thickness range to avoid substrate influence [28]. The contact area function was calibrated using fused silica as a reference material. A minimum of 100 indentations were measured per sample.

Hardness (H_B) and reduced Young's modulus (E_r) were calculated from the load–displacement curves following the Oliver and Pharr's method [28]. The contact stiffness (S) was extracted from the initial unloading slope:

$$S = \frac{dP}{dh} \tag{1}$$

Where P is the applied load and h is the penetration depth. The reduced Young's modulus E_r was calculated according to:

$$E_r = \frac{S\sqrt{\pi}}{2\beta\sqrt{A}} \tag{2}$$

Here, A is the projected contact area and $\beta = 1.034$ is a correction factor for the Berkovich geometry. The reduced elastic modulus accounts for the elastic displacements of both the indenter and the sample, and is related to the true modulus E by:

$$\frac{1}{E_r} = \frac{1-\nu^2}{E} + \frac{1-\nu_i{}^2}{E_i} \tag{3}$$

where ν and E are the Poisson's ratio and Young's modulus of the film, respectively, while ν_i= 0.07 and $E_i = 1140$ GPa are the corresponding values for the diamond tip. Given the high stiffness of the diamond, E_r closely approximates the actual modulus for most metallic films. Hardness H_B was determined from the maximum load P_{max} and contact area as:

$$H_B = \frac{P_{\max}}{A} \tag{4}$$

Elastic and total indentation work, W_{elast} and W_{total}, were evaluated by integrating the area under the unloading and loading segments of the load-depth curves, respectively. From both results, W_{plast} can be extrapolated as the difference between the values:

$$W_{elast} = \int_{h_{final}}^{h_{\max}} P_{unloading}(h)dh \tag{5}$$

$$W_{total} = \int_{0}^{h_{\max}} P_{loading}(h)dh \tag{6}$$

$$W_{plast} = W_{total} - W_{elast} \tag{7}$$

From this, the plasticity index (W_{plast}/W_{total}) and the elastic recovery (W_{elast}/W_{total}) can be computed.

2.4. Magnetic measurements

In-plane magnetic hysteresis loops and first order reversal curves (FORCs) were measured using a vibrating sample magnetometer (VSM) at room temperature (RT). FORC measurements were conducted using a saturation field of 5 kOe. In each of these measurements, the sample was first saturated at 5 kOe, after which the field was reduced to a reversal field H_r. From this point, the field was swept back to H_{max} while recording the magnetization M, completing one FORC. This procedure was repeated by progressively decreasing H_r (i.e., greater field in absolute value, but towards the opposite direction of H_{max}) until $-H_{max}$ to obtain a complete set of FORCs. Magnetization vs. temperature curves were acquired by swiping the temperature from 100 K up to 700 K, at a 5 K/min rate, under a 5 kOe applied field [29,30].

3. Results

3.1. Morphological and structural characterization

The morphology of the electrodeposited dense and colloidally templated porous samples was evaluated by means of FESEM, with the latter analyzed after the removal of the PS spheres. Representative images of dense and porous Ni and Ni–W films are displayed in Fig. 1. It can be observed that the synthesized dense Ni films exhibit a compact and continuous nanostructured surface composed of cauliflower shaped colonies. The colony boundaries are clearly discernible. The Ni sample templated from the 20 nm PS spheres retains a surface morphology similar to that of the dense film, with the additional presence of mesopores. In contrast, for the Ni sample templated from the 200 nm PS spheres, the morphology is primarily governed by the induced porosity rather than by the deposition conditions, as is the case for the dense counterpart. Larger pores, uniformly distributed across a smoother

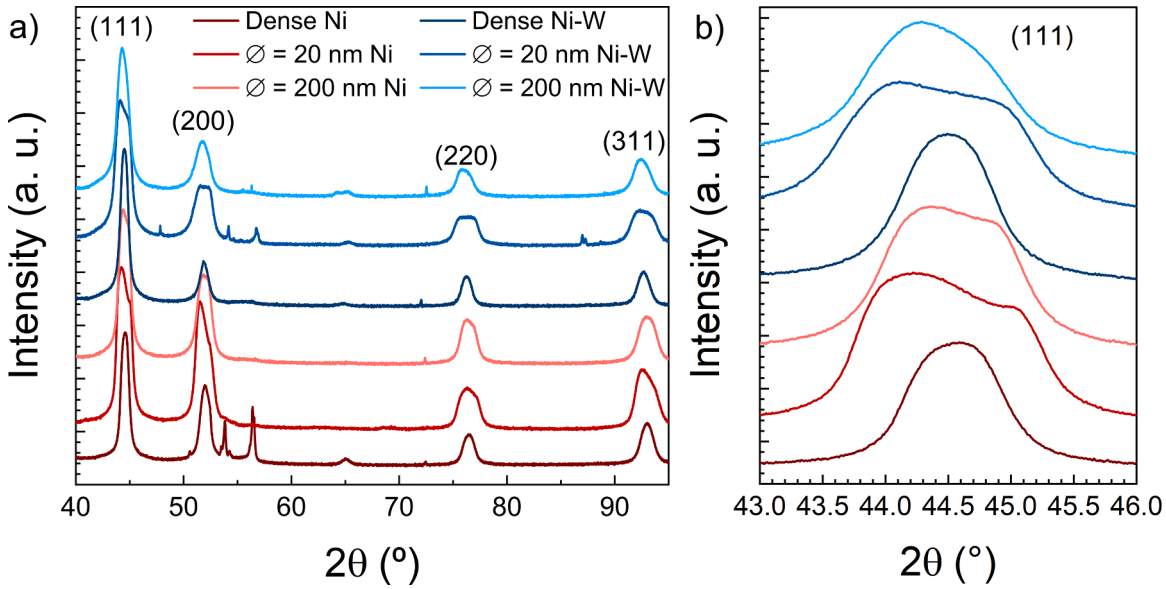

Fig. 2. (a) GIXRD patterns and (b) detailed view of the Ni(111) peak of all electrodeposited samples. Pure Ni films are shown in red (from dark to light: dense, 20 nm pore size, and 200 nm pore size), while Ni–W films are shown in blue following the same order, from dark to light: dense, 20 nm pore size, and 200 nm pore size.

surface, are observed.

The dense Ni–W sample shows a very different morphology to its Ni counterpart (Fig. 1). The surface is also composed of colonies, but these present an acicular morphology, as previously observed [31]. This acicular morphology is accompanied by a significantly lower surface roughness, as measured by AFM (5 nm as compared to 22 nm for dense Ni film, see Supplementary Information, Table S1). The Ni–W sample templated from the 20 nm PS spheres, contrarily to the analogous mesoporous Ni sample, loses the acicular morphology observed in the dense film. The morphology becomes dominated by the templated porosity, which disrupts the original microstructure. Similarly, the Ni–W films templated from the 200 nm PS spheres present a morphology totally controlled by the porosity, as in the case of the Ni counterpart. As expected, the pore diameters in the porous films correspond closely to the size of the PS spheres used during fabrication (Supplementary Information, Fig. S1). For simplicity, we refer to the porous films by the corresponding nominal PS sphere diameters (Ø) from this point onward. AFM measurements reveal that the incorporation of small pores (20 nm) in the films causes an increase in roughness (from 22 nm to 33 nm for the Ni case, and from 5 nm to 34 nm for the Ni–W case), as the mesoporosity superimposes to the grain morphology seen in the dense films (see Table S1 in the Supplementary Information). The roughness of the films with 200 nm pores is lower than that of their mesoporous counterparts, likely because the macropores are not as deep as 200 nm.

The composition of the Ni and Ni–W samples was determined by ICP-OES. Disregarding oxygen, the Ni samples are 100 % Ni, as expected, while the Ni–W films contain the following wt% tungsten: 6.8 (dense), 5.8 (20 nm pores) and 9.3 (200 nm pores). In EDX experiments, the amount of oxygen was low (less than 1 wt% in the dense films and a bit higher in the porous counterparts, of around 2–4 wt.).

The samples were structurally characterized by means of GIXRD and the obtained patterns are shown in Fig. 2a. All films display multiple diffraction peaks that can be unambiguously indexed in the context of a face-centered-cubic (fcc) Ni phase (PDF 00–001–1260) [32], evidencing their polycrystalline character. The unlabeled narrow peaks are attributed to the Si substrate (PDF 00–002–0561) and the Au seed layer (PDF 00–001–1172). The lack of other phases confirms the proper alloying of Ni and W, ruling out W segregation. It is worth noting that the peak positions for the Ni–W samples are shifted towards lower 2θ angles compared to their Ni counterparts, indicating a lattice expansion due to W incorporation into the Ni matrix (Fig. 2a and Table 1). This shift evidences the formation of a metastable Ni–W solid solution extending beyond the equilibrium solubility limit [33,34]. The reduction of stacking-fault energy caused by W addition promotes planar stacking faults and nanocrystalline growth, in agreement with previous observations [33]. The porous architecture further modulates grain size since thinner pore walls (as typically happens in arrangements of larger spheres) restrict grain growth.

A pronounced peak splitting of the Ni(W) fcc phase is observed for all porous films, both for pure Ni and Ni–W samples. This effect is related to

Table 1
Cell parameter, a, crystal size, $<D>$, microstrains, ε, and phase percentages obtained from Rietveld refinement of the full XRD patterns of Fig. 2. The associated error for a is 10^{-3} while that of <D> and ε is 10 %.

Sample	fcc-1				fcc-2			
	a (Å)	<D> (nm)	ε (10^{-3})	vol%	a (Å)	<D> (nm)	ε (10^{-3})	vol%
Dense Ni	3.526	38	3.4	100	–	–	–	–
Ø = 20 nm Ni	3.523	46	5.3	86	3.470	30	2.0	14
Ø = 200 nm Ni	3.524	28	4.7	93	3.482	41	0.2	7
Dense Ni–W (6.8 wt% W)	3.539	37	3.0	100	–	–	–	–
Ø = 20 nm Ni–W (5.8 wt% W)	3.552	17	3.4	90	3.507	23	4.1	10
Ø = 200 nm Ni–W (9.3 wt% W)	3.541	17	3.4	93	3.506	40	0.3	7

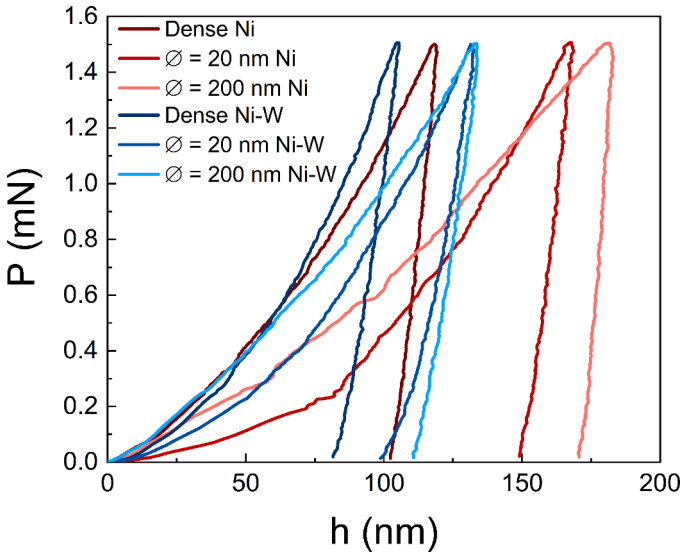

Fig. 3. Representative load-depth nanoindentation curves for all the investigated films (red corresponds to Ni films, blue to Ni–W films).

the existence of two fcc phases with slightly different lattice constant (Fig. 2b). If we look at the Ni samples, one of the observed phases (denoted as fcc-1) has a lattice constant consistent with bulk Ni (a = 3.52 Å), while the other phase (denoted as fcc-2) shows a lower cell constant, indicating a contracted lattice (Table 1). This contraction is likely associated with regions of material that formed inside or deep within the pore walls surrounding the PS spheres during growth, which would have been subject to compressive strain [35]. The same can be said for the Ni-W films, where the fcc-2 phase has a lower cell parameter than the fcc-1 phase. All films are nanostructured, as evidenced by the crystallite size which lies between 17 nm and 46 nm.

The phase percentages indicate that the fcc-1 is the major phase, amounting to 86–93 % of the whole film volume. Rietveld refinement of the XRD patterns further reveals that the microstrains in the major fcc-1 phase increase with porosity (Table 1), confirming that confined or restricted growth results in a higher concentration of lattice distortions compared to growth on planar substrates. The microstrain values for the dense Ni film are comparable to those reported in other studies on electroplated nickel [36]. On the other hand, the diffractograms of the porous samples show significantly higher backgrounds (i.e., halos in the 2θ interval 40 – 55°) which may indicate the additional presence of an amorphous phase, such as Ni oxide /hydroxide (see Fig. S2, Supplementary Information). Due to their higher surface-to-volume ratio, porous films are expected to exhibit a more pronounced passivation phenomenon.

3.2. Mechanical properties

A series of nanoindentation experiments were conducted on the films using a 1.5 mN indentation force to ensure reliable results that are not influenced by the mechanical properties of the underlying substrates (Fig. 3). The results obtained from the nanoindentation tests were used to calculate mechanical parameters, such as hardness and Young's modulus, by applying the method of Oliver and Pharr [28]. The results obtained for all samples, whose thickness was $\geq$ 1.5 µm, are summarized in Table 2. The dense Ni–W film exhibited the highest hardness with 4.4 ± 0.4 GPa. This value is lower than that reported for hard chromium coatings, whose hardness can be as high as 9–14 GPa [37,38]. The hardness of Ni–W alloys can be increased by raising the tungsten content, although this comes at the cost of a reduced magnetization (see next section). Therefore, further enhancing mechanical hardness compromises soft-ferromagnetic performance, highlighting a clear trade-off between these two physical properties. Despite their moderate hardness, Ni-W films may remain a viable coating option due to their lower friction coefficient, as reported in previous studies [39].

A decrease in hardness was observed in the porous Ni–W samples reaching 2.8 ± 0.6 and 2.9 ± 0.6 GPa for pore sizes of 20 and 200 nm, respectively. This trend reflects the effect of porosity on the mechanical properties of the films, i.e., a microstructural softening. In contrast, pure

Table 2
Hardness (H_B), reduced elastic modulus (E_r), elastic recovery, and plasticity index for all electrodeposited samples.

Sample	Dense Ni	Ø = 20 nm Ni	Ø = 200 nm Ni	Dense Ni–W	Ø = 20 nm Ni–W	Ø = 200 nm Ni–W
H_B (GPa)	3.7 ± 0.6	2.0 ± 0.2	1.7 ± 0.3	4.4 ± 0.4	2.8 ± 0.6	2.9 ± 0.6
E_r (GPa)	173 ± 46	147 ± 25	92 ± 48	150 ± 18	130 ± 40	115 ± 25
Elastic recovery (%)	16 ± 5	12 ± 3	18 ± 12	20 ± 2	20 ± 6	17 ± 3
Plasticity index (%)	84 ± 5	88 ± 3	82 ± 12	80 ± 2	80 ± 6	83 ± 3

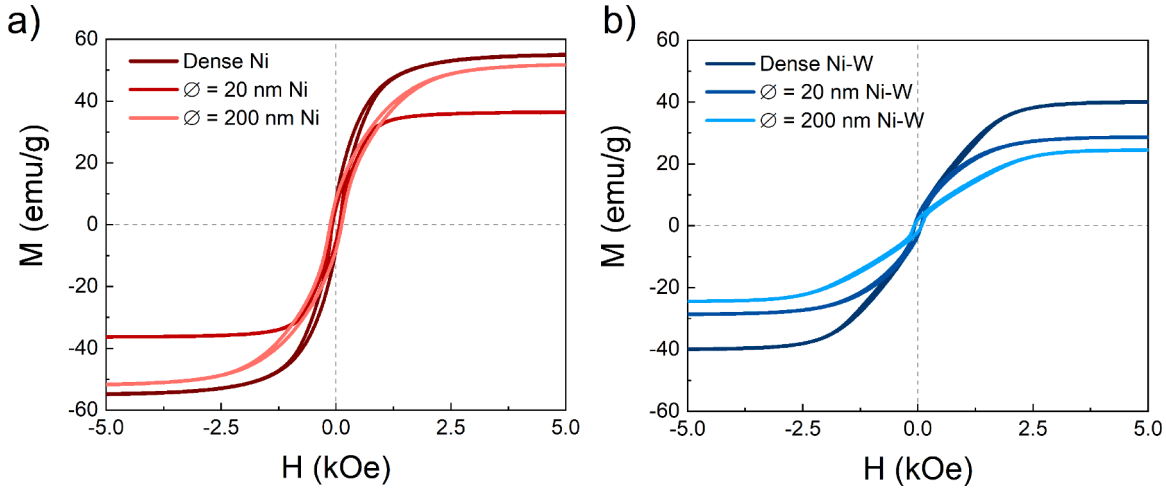

Fig. 4. In-plane hysteresis loops for (a) Ni and (b) Ni–W films.

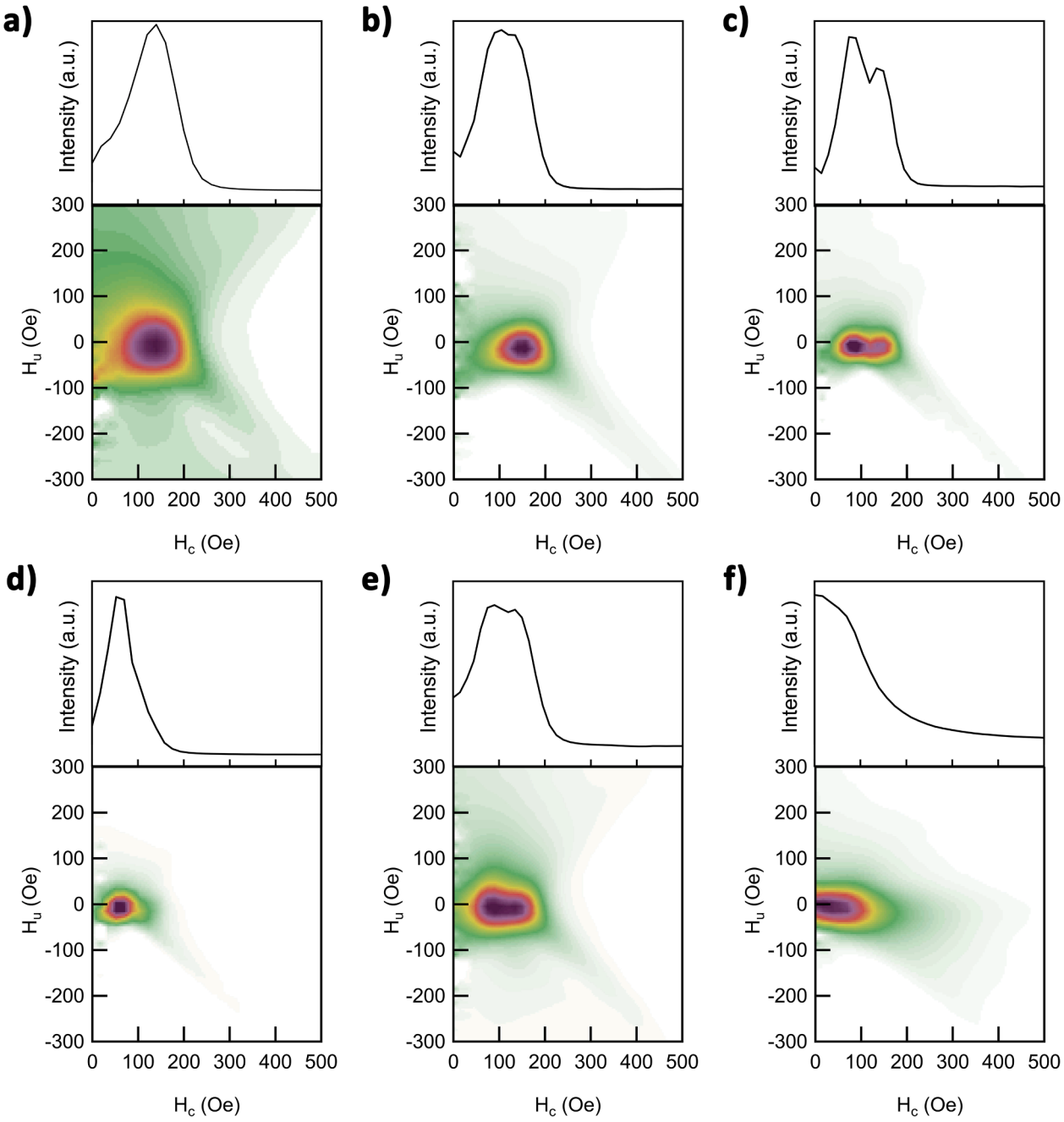

Fig. 5. First order reversal curves and horizontal section of relative intensity of the (a) dense, (b) porous with 20 nm pore size and (c) porous with 200 nm pore size pure Ni films, and (d) dense, (e) porous with 20 nm pore size and (f) porous with 200 nm pore size Ni–W films.

Ni samples showed much lower hardness values, with only 3.7 ± 0.6 GPa for dense, 2.0 ± 0.2 for the mesoporous (Ø = 20 nm) and 1.7 ± 0.3 GPa for the macroporous (Ø = 200 nm) samples. Overall, the effect of W alloying is an enhancement in hardness for all morphologies due to solid solution strengthening, as previously seen in literature [40]. The reduced Young's modulus follows a similar trend as the hardness with porosity. The dense films reach the highest values at 173 ± 43 GPa and 150 ± 18 GPa for Ni and Ni–W, respectively. They are then followed by a sharp drop of about 20 GPa in the mesoporous (Ø = 20 nm) films, further decreasing in the macroporous (Ø = 200 nm) samples.

Finally, the elastic recovery and plasticity index remain relatively stable across all samples with around 80 % for the plasticity index, suggesting that the general deformation mechanism does not change drastically neither by alloying with W, nor by modifying the film microstructure, although slightly higher plasticity is observed in porous pure Ni films.

3.3. *Magnetic measurements*

Magnetic properties of the synthesized samples were investigated using a VSM. The obtained results are mass-normalized to minimize volume-related errors in the porous films, as the true surface area of the samples is difficult to determine. Fig. 4 shows the in-plane hysteresis loops recorded at RT for all samples. It is worth noting that some of the loops (e.g., the dense Ni–W and the porous films) have shapes that suggest superposition of different magnetic contributions. Pure Ni films (Fig. 4a) show saturation magnetization values (M_S) of 55.4 emu/g, 36.5 emu/g, and 52.3 emu/g for the dense, mesoporous (Ø = 20 nm) and macroporous (Ø = 200 nm) samples, respectively (see Table S2 in the Supplementary information). The value for dense Ni matches M_S of

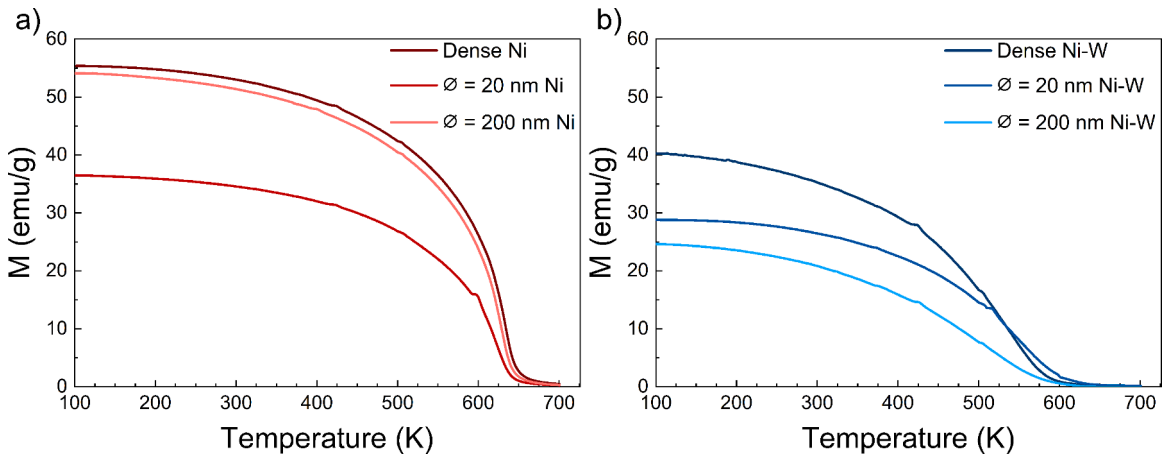

Fig. 6. Dependence of the magnetization (mass normalized) with temperature for (a) Ni and (b) Ni–W films.

bulk Ni reported in the literature [41]. The differences observed when introducing porosity to the Ni film can be explained considering a more pronounced surface oxidation of the porous films as discussed already from the background seen in the corresponding XRD patterns. Indeed, the effect of this passivation is more pronounced in the samples with pore size of 20 nm due to their higher surface-to-volume ratio compared to those with 200 nm pores (Fig. 1).

On the other hand, all the Ni–W samples exhibit lower M_S values than their Ni counterparts. While oxidation may also play a role in this reduction, this cannot be the only cause for this effect. Namely, its M_S already drops by 15.1 emu/g compared to dense Ni with only 6.8 wt% W. Similarly, the M_S of the porous films decreases by 11.5 emu/g for the mesoporous (Ø = 20 nm) sample (5.8 wt% W) and by 15.6 emu/g for the macroporous (Ø = 200 nm) (9.3 wt% W) film. Conversely, in the porous Ni films, M_S drops by 18.9 emu/g for the mesoporous (Ø = 20 nm) and 3.1 emu/g for the macroporous (Ø = 200 nm) samples, thus the behavior in both types of samples (Ni vs. Ni-W) is different (Table S2). If oxidation was the only phenomenon detrimental to the magnetism of the samples, the drop in M_S associated to passivation due to the introduction of porosity should be comparable between Ni and Ni–W samples. The effect of alloying Ni with W on M_S can be as significant or even overcome the passivation effect. Since W is paramagnetic, its incorporation into Ni disrupts the ferromagnetic exchange interactions [42]. Furthermore, the lower reduction in M_S observed in the mesoporous (Ø = 20 nm) Ni-W sample relative to its Ni counterpart suggests that W helps, in fact, mitigate oxidation, since it forms a W-rich passivating surface layer. Indeed, the oxygen content detected by EDX in the films was 4 wt% for Ni against 2 wt% for Ni-W although it tends to be underestimated.

To further study the multiple magnetic contributions observed in the hysteresis loops, FORC experiments were performed. By measuring minor loops of the sample, this technique allows to disentangle the different contributions observed in the major loop [43,44]. The FORC distribution maps are displayed in Fig. 5a-c for pure Ni and Fig. 5d-f for Ni-W, alongside a horizontal intensity profile (along H_C axis). The dense Ni film (Fig. 5a) displays a single well-defined peak centered at H_C = 140 Oe, indicative of homogeneous magnetic behavior. Contrarily, when analyzing the horizontal profile of the porous Ni films, these exhibit two distinct coercivity distributions: a peak similar to the dense sample (at H_C = 140 Oe), and a second peak reflecting an additional magnetic contribution at lower H_C values. This additional contribution becomes more evident as the size of the pores becomes larger, suggesting an additional shape anisotropy originating from the introduction of porosity into the sample. Indeed, this contribution is consistent with the deposition method applied to induce porosity. The PS spheres form a compacted-like structure, and the Ni and Ni–W deposits around them. This can lead to thin walls between neighboring spheres, which may become locally thinner when the spheres are bigger and in close contact, eventually reaching small enough sizes to form regions with large shape anisotropy or even single domain clusters. It is worth noting that the coercivity of the hysteresis loops does not always precisely match the coercivity distribution from the FORC diagrams. This effect has been previously reported [45,46], and therefore the FORC analysis must be taken mainly as semi-quantitative.

A similar trend can be noticed for the Ni–W samples. While the dense film shows a single distinct peak at H_C= 60 Oe, the mesoporous (Ø = 20 nm) Ni-W sample features two separate peaks, even in a more evident manner than in the case of pure Ni. However, the macroporous (Ø = 200 nm) Ni–W sample exhibits a peculiar FORC distribution. The coercivity distribution extends from H_C = 0 Oe to about 140 Oe, indicating the coexistence of superparamagnetic and multi-domain grains within the film. Similar effects have also been observed in previous works of electrodeposited Ni films (with and without pores) [29,45]. Two factors may help explain why this effect is observed only in this sample: the incorporation of W, and the reduced wall thickness (<30 nm) between neighbouring pores likely resulting from the use of larger, locally compacted, PS spheres. The detrimental impact of W alloying with Ni on the films' ferromagnetic properties is amplified in regions with very small dimensions (such as pore walls), where superparamagnetism and other size-dependent effects can emerge at room temperature [47,48].

Moment versus temperature (M vs. T) curves were measured to assess the effects of alloying and film morphology on the T_C of the samples. These curves, in the range from 100 K to 700 K, are shown in Fig. 6. The obtained T_C values are tabulated in Table S2 of the Supplementary Information. All three pure Ni samples (Fig. 6a) exhibit similar T_C of 652 K, 643 K and 649 K for dense and porous (Ø = 20 nm, 200 nm) samples, respectively, slightly higher than the commonly reported value for bulk Ni ($T_{C,Nibulk}$ = 630 K) [49]. Conversely, the Ni–W samples (Fig. 6b) show lower T_C values, of 589 K, 607 K and 585 K for the dense, mesoporous (Ø = 20 nm) and macroporous (Ø = 200 nm) films. It is worth noting that when the tungsten wt% increases, T_C decreases. These results suggest that structural differences among the films caused by porosity do not strongly affect T_C, whereas the addition of W causes a reduction of T_C by already 40 K with only 6.3 wt% W compared to the bulk value for Ni. This behavior is consistent with previous reports and reflects the dilution of the magnetic Ni matrix by paramagnetic W atoms, weakening the ferromagnetic exchange interactions and, consequently, lowering T_C [50].

3.4. *Thermal stability of the porous films*

The stability of the porous films at high temperatures was assessed by FESEM after successive annealing treatments (in steps of 100 K) in an inert Ar atmosphere up to 800 K. Fig. 7 shows the FESEM images for all

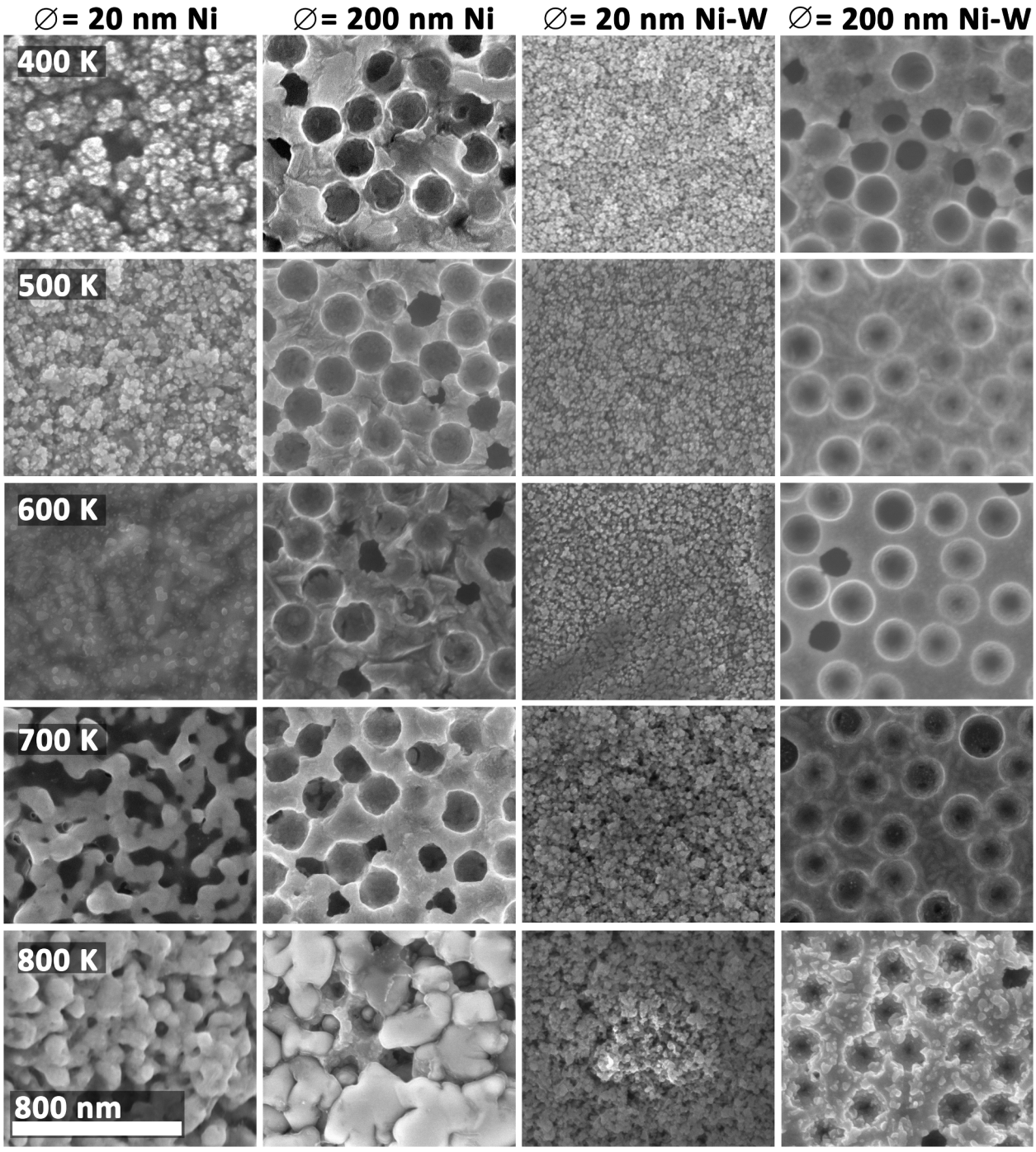

Fig. 7. FESEM images of mesoporous Ni (Ø = 20 nm) (first column), macroporous Ni (Ø = 200 nm) (second column), mesoporous Ni–W (Ø = 20 nm) (third column) and macroporous Ni–W (Ø = 200 nm) (fourth column) after successively annealing the samples at temperatures ranging from 400 K to 800 K (ordered in descending rows) in Ar atmosphere. Scale bar the is the same for all images.

porous samples after every annealing step (i.e., after annealing at 400 K, 500 K, 600 K, 700 K and 800 K). Samples remained morphologically stable up to 600 K. At this temperature, signs of pore coalescence started to become noticeable in the mesoporous Ni (Ø = 20 nm) sample. The posterior annealing at 700 K proved fatal for this sample, and signs of pore collapsing have already started in the macroporous (Ø = 200 nm) Ni sample. Finally, after heating to 800 K, significant morphological changes were detected in the pure Ni films, which completely lost the initial morphology. In contrast, the mesoporous Ni–W (Ø = 20 nm) samples remained largely unchanged throughout the consecutive annealing routines, demonstrating excellent thermal stability. The macroporous Ni–W (Ø = 200 nm) films showed the growth of crystalline features atop the porous surface at 800 K, suggesting partial recrystallization, although the pores were still obvious and well maintained. This demonstrates the beneficial influence of W in Ni–W to preserve porosity after high-temperature treatments.

4. Conclusions

Nanostructured Ni and Ni–W alloy films with both dense and porous architectures have been successfully electrodeposited, the porous structures fabricated using a colloidal templating strategy. Structural

characterization confirmed the nanocrystalline nature of all samples and revealed the coexistence of two fcc phases in the porous films: one with a lattice parameter close to that of bulk Ni, and another with a contracted lattice, indicative of compressive strain. Mechanical characterization revealed that while W alloying with Ni leads to consistent increase in hardness due to solid solution strengthening, the introduction of porosity significantly reduces hardness and Young's modulus.

Magnetic hysteresis loops show a systematic decrease in M_S with increasing W content and porosity, consistent with magnetic dilution and increased surface oxidation of the porous films. The porous structures give rise to an additional magnetic contribution as discerned by FORC measurements through the occurrence of multiple peaks in the H_C distribution. This additional contribution is related to surface or shape anisotropy. In addition, the macroporous Ni–W (Ø = 200 nm) film shows a superparamagnetic contribution attributed to isolated magnetic clusters formed within the very thin pore walls. Incorporation of W into Ni–W causes a clear decrease of T_C, while porosity has a negligible influence on T_C.

Our results also reveal that, unlike pure Ni films whose porous structure degrades above 600 K, the Ni–W films remain morphologically stable up to 800 K, confirming a superior thermal stability. These results evidence that both composition and porosity in nanostructured Ni–W films can be tailored in a controlled manner, making these materials promising candidates for multifunctional MEMS applications and sustainable alternatives for Cr-based coatings.

CRediT authorship contribution statement

Roger de Paz-Castany: Writing – original draft, Visualization, Validation, Methodology, Investigation, Formal analysis, Data curation. **Nicolau López-Pintó:** Writing – review & editing, Visualization, Validation, Software, Methodology, Investigation, Formal analysis, Data curation. **Konrad Eiler:** Writing – review & editing, Investigation, Formal analysis. **Stenning Gavin B. G.:** Investigation. **Annick Hubin:** Writing – review & editing, Supervision, Project administration. **Eva Pellicer:** Writing – review & editing, Supervision, Resources, Project administration, Funding acquisition, Conceptualization. **Jordi Sort:** Writing – review & editing, Resources, Methodology, Conceptualization.

Declaration of Competing Interest

The authors declare that they have no known competing financial interests or personal relationships that could have appeared to influence the work reported in this paper.

Acknowledgements

This work has received funding from the European Union's HORIZON Research and Innovation Actions under grant agreement No. 101058076 – NICKEFFECT. Views and opinions expressed are however those of the authors only and do not necessarily reflect those of the European Union or European Health and Digital Executive Agency (HaDEA). Neither the European Union nor HaDEA can be held responsible for them. Financial support by the Generalitat de Catalunya (2021-SGR-00651), and the Spanish Government (PID2020–116844RB-C21) are also acknowledged. We would like to thank the Materials Characterisation Laboratory at the ISIS Neutron and Muon Source for help on the GIXRD instrument.

Appendix A. Supporting information

Supplementary data associated with this article can be found in the online version at doi:10.1016/j.jallcom.2025.184863.

References

[1] W.J. Dera, H. Konopacka, D.M. Jarząbek, Development of a novel nickel-based metal force microsensor using bottom-up approach, Precis Eng. 95 (2025) 251–261, https://doi.org/10.1016/j.precisioneng.2025.05.003.
[2] E. Gasparin, A. Hoogerwerf, D. Bayat, G.S. Durante, Y. Petremand, M. Tormen, M. Despont, G. Close, Design of an integrated MEMS magnetic gradiometer rejecting vibrations and stray fields, IEEE J. Electron Devices Soc. 13 (2025) 228–236, https://doi.org/10.1109/JEDS.2025.3543662.
[3] J.W. Kim, M. Salauddin, H. Cho, M.S. Rasel, J.Y. Park, Electromagnetic energy harvester based on a finger trigger rotational gear module and an array of disc Halbach magnets, Appl. Energy 250 (2019) 776–785, https://doi.org/10.1016/j.apenergy.2019.05.059.
[4] W. Schwarzacher, K. Attenborough, A. Michel, G. Nabiyouni, J.P. Meier, Electrodeposited nanostructures, J. Magn. Magn. Mater. 165 (1997) 23–29, https://doi.org/10.1016/S0304-8853(96)00465-9.
[5] T. Borkar, S.P. Harimkar, Effect of electrodeposition conditions and reinforcement content on microstructure and tribological properties of nickel composite coatings, Surf. Coat. Technol. 205 (2011) 4124–4134, https://doi.org/10.1016/j.surfcoat.2011.02.057.
[6] K. Dev, A. Kadian, V.R. Reddy, R. Medwal, S. Annapoorni, Magnetization switching dynamics of electrodeposited Fe–Ni thin films, J. Supercond. Nov. Magn. 37 (2024) 1243–1255, https://doi.org/10.1007/s10948-024-06766-x.
[7] X. Liu, G. Zangari, L. Shen, Electrodeposition of soft, high moment Co–Fe–Ni thin films, J. Appl. Phys. 87 (2000) 5410–5412, https://doi.org/10.1063/1.373359.
[8] M.M. Abou-Krisha, H.M. Rageh, E.A. Matter, Electrochemical studies on the electrodeposited Zn–Ni–Co ternary alloy in different media, Surf. Coat. Technol. 202 (2008) 3739–3746, https://doi.org/10.1016/j.surfcoat.2008.01.015.
[9] R. Yang, H. Xie, Y. Sun, W. Huang, Y. Fang, J. Liu, Codeposition behavior of Fe–Ni alloys: A review in mechanisms, preparation and effects on composition, Mater. Sci. Eng. B 310 (2024) 117723, https://doi.org/10.1016/j.mseb.2024.117723.
[10] A. Karpuz, H. Kockar, M. Alper, Scanning of nickel sulfamate concentration in electrodeposition bath used for production of Ni–Co alloys, J. Mater. Sci. Mater. Electron 24 (2013) 3376–3381, https://doi.org/10.1007/s10854-013-1258-3.
[11] H. Kockar, M. Alper, O. Karaagac, N. Nakiboglu, M.C. Baykul, Contribution of electrolyte pH and deposition potentials to the magnetic anisotropy of electrodeposited nickel films, J. Magn. Magn. Mater. 322 (2010) 1088–1091, https://doi.org/10.1016/j.jmmm.2009.11.038.
[12] M. Bayirli, H. Kockar, M. Alper, E. Cokturen, Determination of texture orientation related magnetic properties of nickel–cobalt films, Z. Nat. A 65 (2010) 342–346, https://doi.org/10.1515/zna-2010-0411.
[13] M. Alper, H. Kockar, H. Kuru, T. Meydan, Influence of deposition potentials applied in continuous and pulse waveforms on magnetic properties of electrodeposited nickel–iron films, Sens. Actuators A Phys. 129 (2006) 184–187, https://doi.org/10.1016/j.sna.2005.11.040.
[14] C. Zhang, W. Si, Y. Wang, S. Dai, Da S. Investigations on the influence of annealing on microstructure and mechanical properties of electrodeposited Ni–Mo and Ni–Mo–W alloy coatings, Coatings 11 (2021) 1428, https://doi.org/10.3390/coatings11111428.
[15] N.P. Wasekar, S. Verulkar, M.V.N. Vamsi, G. Sundararajan, Influence of molybdenum on the mechanical properties, electrochemical corrosion and wear behavior of electrodeposited Ni–Mo alloy, Surf. Coat. Technol. 370 (2019) 298–310, https://doi.org/10.1016/j.surfcoat.2019.04.059.
[16] S. Lee, M. Choi, S. Park, H. Jung, B. Yoo, Mechanical properties of electrodeposited Ni–W thin films with alternate W-rich and W-poor multilayers, Electro Acta 153 (2015) 225–231, https://doi.org/10.1016/j.electacta.2014.11.190.
[17] K. Shekhawat, S. Chatterjee, B. Joshi, Chromium toxicity and its health hazards, Int. J. Adv. Res. 3 (2015) 167–172.
[18] T.L. DesMarias, M. Costa, Mechanisms of chromium-induced toxicity, Curr. Opin. Toxicol. 14 (2019) 1–7, https://doi.org/10.1016/j.cotox.2019.05.003.
[19] G.G.E. Low, M.F. Collins, Magnetic moment distributions in dilute nickel alloys, J. Appl. Phys. 34 (1963) 1195–1199, https://doi.org/10.1063/1.1729431.
[20] V.N. Jafarova, N.N. Hashimova, I.C. Scurtu, High Curie temperature in Zn(Co,Ni)Se: DFT study, Tech. Rom. J. Appl. Sci. Technol. 25 (2024) 142–147, https://doi.org/10.47577/technium.v25i.12148.
[21] T. Heine, M. Dinca, G. Zhou, Physical phenomena in porous frameworks, Acc. Chem. Res 58 (2025) 327–329, https://doi.org/10.1021/acs.accounts.4c00835.
[22] H. Jeon, J. Markmann, S. Shi, Effects of structural hierarchy and size on mechanical behavior of nanoporous gold, Acta Mater. 273 (2024) 119954, https://doi.org/10.1016/j.actamat.2024.119954.
[23] C. Hitz, A. Lasia, Experimental study and modeling of impedance of the HER on porous Ni electrodes, J. Electro Chem. 500 (2001) 213–222, https://doi.org/10.1016/S0022-0728(00)00317-X.
[24] I. Herraiz-Cardona, E. Ortega, L. Vázquez-Gómez, V. Pérez-Herranz, Double-template fabrication of three-dimensional porous nickel electrodes for hydrogen evolution reaction, Int. J. Hydrog. Energy 37 (2012) 2147–2156, https://doi.org/10.1016/j.ijhydene.2011.09.155.
[25] C.H. Liao, P.S. Hung, Y. Cheng, S.Y. Chang, P.W. Wu, Mechanical properties of three-dimensional ordered macroporous Ni foam, Mater. Lett. 215 (2018) 152–156, https://doi.org/10.1016/j.matlet.2017.12.087.
[26] L. Lutterotti, P. Scardi, Simultaneous structure and size–strain refinement by the Rietveld method, J. Appl. Crystallogr. 23 (1990) 246–252, https://doi.org/10.1107/S0021889890002382.
[27] Lutterotti L. MAUD – Materials analysis using diffraction (and more). GitHub. ⟨https://luttero.github.io/⟩ Accessed 5 Jul 2025.

[28] W.C. Oliver, G.M. Pharr, An improved technique for determining hardness and elastic modulus using load and displacement sensing indentation experiments, J. Mater. Res 7 (1992) 1564–1583, https://doi.org/10.1557/jmr.1992.1564.
[29] F. Nasirpouri, H. Cheshideh, A.Y. Samardak, A.V. Ognev, A.A. Zubkov, A. S. Samardak, Morphology- and magnetism-controlled electrodeposition of Ni nanostructures on TiO_2 nanotubes for hybrid Ni/TiO_2 functional applications, Ceram. Int 45 (2019) 11258–11269, https://doi.org/10.1016/j.ceramint.2019.02.200.
[30] I.D. Mayergoyz, Hysteresis models from the mathematical and control theory points of view, J. Appl. Phys. 57 (1985) 3803–3805, https://doi.org/10.1063/1.334925.
[31] R. de Paz-Castany, K. Eiler, A. Nicolenco, M. Lekka, E. García-Lecina, G. Brunin, G. M. Rignanese, D. Waroquiers, T. Collet, A. Hubin, E. Pellicer, Hydrogen evolution reaction of electrodeposited Ni-W films in acidic medium and performance optimization using machine, learning 18 (2025) e202400444, https://doi.org/10.1002/cssc.202400444.
[32] J.D. Hanawalt, H.W. Rinn, L.K. Frevel, Chemical analysis by X-ray diffraction, Ind. Eng. Chem. Anal. Ed. 10 (1938) 457–512.
[33] U. Welzel, J. Kümmel, E. Bischoff, S. Kurz, E.J. Mittemeijer, Nanoscale planar faulting in nanocrystalline Ni–W thin films: grain growth, segregation, and residual stress, J. Mater. Res 26 (2011) 2558–2573, https://doi.org/10.1557/jmr.2011.238.
[34] T.D. Ziebell, C.A. Schuh, Residual stress in electrodeposited nanocrystalline nickel–tungsten coatings, J. Mater. Res 27 (2012) 1271–1284, https://doi.org/10.1557/jmr.2012.51.
[35] G. Abbondanza, A. Larsson, W. Linpé, C. Hetherington, F. Carlá, E. Lundgren, G. S. Harlow, Templated electrodeposition as a scalable and surfactant-free approach to the synthesis of Au nanoparticles with tunable aspect ratios, Nanoscale Adv. 4 (2022) 2452–2467, https://doi.org/10.1039/d2na00188h.
[36] F. Dalla Torre, H. Van Swygenhoven, M. Victoria, Nanocrystalline electrodeposited Ni: Microstructure and tensile properties, Acta Mater. 50 (2002) 3957–3970, https://doi.org/10.1016/S1359-6454(02)00198-2.
[37] A. Almotairi, A. Warkentin, Z. Farhat, Mechanical damage of hard chromium coatings on 416 stainless steel, Eng. Fail Anal. 66 (2016) 130–140, https://doi.org/10.1016/j.engfailanal.2016.04.011.
[38] R. Guillon, O. Dalverny, B. Fori, C. Gazeau, J. Alexis, Mechanical behaviour of hard chromium deposited from a trivalent chromium bath, Coatings 12 (2022) 354, https://doi.org/10.3390/coatings12030354.
[39] C.A. Schuh, T.G. Nieh, H. Iwasaki, The effect of solid solution W additions on the mechanical properties of nanocrystalline Ni, Acta Mater. 51 (2003) 431–443, https://doi.org/10.1016/S1359-6454(02)00427-5.
[40] S. Kirihara, Y. Umeda, K. Tashiro, H. Honma, O. Takai, Development of Ni–W alloy plating as a substitution of hard chromium plating, Trans. Mater. Res. Soc. Jpn 41 (2016) 35–39, https://doi.org/10.14723/tmrsj.41.35.
[41] M.J. Aus, B. Szpunar, A.M. El-Sherik, U. Erb, G. Palumbo, K.T. Aust, Magnetic properties of bulk nanocrystalline nickel, Scr. Met. Mater. 27 (1992) 1639–1643, https://doi.org/10.1016/0956-716X(92)90158-B.
[42] F.A. Khan, M.A. Asgar, P. Nordblad, Magnetization and magnetocrystalline anisotropy of Ni–Mo single crystal alloys, J. Magn. Magn. Mater. 174 (1997) 121–126, https://doi.org/10.1016/S0304-8853(97)00182-0.
[43] D.A. Gilbert, P.D. Murray, J. De Rojas, R.K. Dumas, J.E. Davies, K. Liu, Reconstructing phase-resolved hysteresis loops from first-order reversal curves, Sci. Rep. 11 (2021) 4018, https://doi.org/10.1038/s41598-021-83349-z.
[44] Y.G. Velázquez, A.L. Guerrero, J.M. Martínez, E. Araujo, M.R. Tabasum, B. Nysten, L. Piraux, A. Encinas, Relation of the average interaction field with the coercive and interaction field distributions in first-order reversal curve diagrams of nanowire arrays, Sci. Rep. 10 (2020) 78279, https://doi.org/10.1038/s41598-020-78279-1.
[45] F. Nasirpouri, S. Barzegar, A.Y. Samardak, A.V. Ognev, A.A. Zubkov, A. Stancu, A. S. Samardak, Mesophase micelle-assisted electrodeposition and magnetisation behavior of mesoporous nickel films for efficient electrochemical energy and magnetic device applications, Appl. Surf. Sci. 471 (2019) 776–785, https://doi.org/10.1016/j.apsusc.2018.12.031.
[46] S. Ruta, O. Hovorka, P.W. Huang, K. Wang, G. Ju, R. Chantrell, First-order reversal curves and intrinsic parameter determination for magnetic materials: limitations of hysteron-based approaches in correlated systems, Sci. Rep. 7 (2017) 45218, https://doi.org/10.1038/srep45218.
[47] J.T. Batley, M. Nguyen, I. Kamboj, C. Korostynski, E.S. Aydil, C. Leighton, Quantitative understanding of superparamagnetic blocking in thoroughly characterized Ni nanoparticle assemblies, Chem. Mater. 32 (2020) 6494–6506, https://doi.org/10.1021/acs.chemmater.0c01758.
[48] A.H. Lu, E.L. Salabas, F. Schüth, Magnetic nanoparticles: synthesis, protection, functionalization and application, Angew. Chem. Int. Ed. 46 (2007) 1222–1244, https://doi.org/10.1002/anie.200602866.
[49] L. Néel, Propriétés magnétiques du nickel pur à proximité du point de Curie, J. De. Phys. Et. Le. Radium 6 (1935) 27–34, https://doi.org/10.1051/jphysrad:019350060102700.
[50] D. Hunter, S.A. Arrott, I.R. Grynszpan, P. Dassonwalle, P. Langlois, Magnetization measurements for dilute alloys of Ni, J. Phys. Colloq. 49 (1988) C8-131–C8-132, https://doi.org/10.1051/jphyscol:1988852.